ANTIDISSIPATIVE NUMERICAL SCHEMES FOR THE ANISOTROPIC DIFFUSION OPERATOR IN PROBLEMS FOR THE ALLEN-CAHN EQUATION

PAVEL STRACHOTA*

Abstract. This contribution discusses two attitudes to artificial dissipation reduction in numerical schemes for solving initial boundary value problems for the Allen-Cahn equation with anisotropy incorporated into the diffusion operator. In the first case, a weighted first order finite difference scheme is used for spatial discretization of the anisotropic texture diffusion problem in 2D, designed for vector field visualization. In the second case, a higher order finite volume scheme is used for the texture diffusion problem in 3D, applied in a MR tractography algorithm. The anisotropy of the diffusion is controlled by the diffusion tensor field. For both problems, comparisons with standard low order schemes are given in the form of pictures, together with remarks on convergence analysis results.

Key words. Allen-Cahn equation, anisotropic diffusion, finite difference method, finite volume method, mathematical visualization, numerical dissipation

AMS subject classifications. 15A15, 15A09, 15A23

1. Introduction.

The Allen-Cahn equation having its origin in phase modeling in physics [1] has since found its application in other fields, including image processing and mathematical visualization [4, 13, 12]. In particular, in order to visualize the streamlines of a given vector or tensor field, an initial boundary value problem for the modified Allen-Cahn equation with incorporated anisotropy can be used (see [13, 12] and [9]). Unfortunately, simple first order schemes for its numerical solution suffer from artificial (numerical) dissipation, i.e. an error demonstrating itself as an additional *isotropic diffusion* and significantly deteriorating the visualization results. In the following sections, we introduce two similar problems for the Allen-Cahn equation in the context of vector and tensor field visualization. For each of them, a different approach aimed at reduction of the artificial diffusion in the numerical solution is proposed.

2. Vector field visualization problem.

Suppose a static vector field $\boldsymbol{v}$ is defined in a rectangular domain $\Omega = (0, L^1) \times (0, L^2)$. Generating a noisy texture in Ω and making it undergo an anisotropic diffusion process with the diffusion focused in the direction $\boldsymbol{v}(\boldsymbol{x})$ at each point $\boldsymbol{x} \in \Omega$, the streamlines of the vector field emerge as "smudges". In addition to smearing, one may impose advection on the texture in order to interpret the flow of the fluid along the vector field.

Formulation. Let $p : \mathcal{J} \times \Omega \mapsto \mathbb{R}$, $p = p(t, \boldsymbol{x})$ be the function of texture intensity at each point $\boldsymbol{x} \in \Omega$ and at the time $t \in \bar{\mathcal{J}}$, where $\mathcal{J} = (0, T)$ is the time interval. The initial boundary value problem for the Allen-Cahn equation with advection (see

---

*Dept. of Mathematics, Faculty of Nuclear Sciences and Physical Engineering, Czech Technical University in Prague, (`pavel.strachota@fjfi.cvut.cz`).

[11]) reads

$$\xi \frac{\partial p}{\partial t} + \xi \boldsymbol{v} \cdot \nabla p = \xi \nabla \cdot T^0 (\nabla p) + \frac{1}{\xi} f_0(p) + c_0 F \qquad \text{in } \mathcal{J} \times \Omega, \qquad (2.1)$$

$$p|_{\partial \Omega} = 0 \qquad \text{on } \mathcal{J} \times \partial \Omega, \qquad (2.2)$$

$$p|_{t=0} = I \qquad \text{in } \Omega, \qquad (2.3)$$

where

$$f_0(p) = p(1-p)\left(p - \frac{1}{2}\right).$$

In (2.1), the term $\nabla \cdot T^0(\nabla p)$ is the anisotropic diffusion operator focusing the diffusion of p into the direction of the vector field. Consider a vector $\boldsymbol{\eta} = (\eta^1, \eta^2)^{\mathrm{T}} \in \mathbb{R}^2$ and denote the coordinates of $\boldsymbol{\eta}$ in the orthonormal basis $(\frac{1}{v}\boldsymbol{v}, \frac{1}{v}\boldsymbol{v}^\perp)$ by $\tilde{\eta}^1, \tilde{\eta}^2$. The operator T^0 is defined as

$$T^0(\boldsymbol{\eta}) = \Phi^0(\boldsymbol{\eta})\Phi^0_\eta(\boldsymbol{\eta}),$$

where

$$\Phi^0(\boldsymbol{\eta}) = \sqrt{\alpha \cdot (\tilde{\eta}^1)^2 + \beta \cdot (\tilde{\eta}^2)^2}, \quad \Phi^0_\eta(\boldsymbol{\eta}) = \begin{pmatrix} \partial_{\eta^1} \Phi^0(\boldsymbol{\eta}) \\ \partial_{\eta^2} \Phi^0(\boldsymbol{\eta}) \end{pmatrix}. \qquad (2.4)$$

The coefficients α, β depend on the vector field and should be chosen such that the absolute value of T^0 is largest in the case when the directions of $\boldsymbol{v}$ and ∇p coincide. Our choice is

$$\alpha = \kappa\left(1 + \sigma |\boldsymbol{v}|\right), \ \beta = \kappa, \quad \kappa, \sigma > 0.$$

The term $\boldsymbol{v} \cdot \nabla p$ in (2.1) causes texture advection [3]. The polynomial f_0 makes *nucleation* occur during the time. In this context, nucleation is a formation of areas where the value of p is near 0 or 1. As described for example in [2], the parameter ξ is proportional to the diffuse interface layer between such areas. ξ is chosen such that it is small in comparison with the dimensions of Ω. The sense of the product $c_0 F$ is related to the problem of mean curvature flow and is explained e.g. in [3]. However, for the purpose of visualization, it is convenient to put $F = 0$ in most cases.

The initial condition $I : \Omega \mapsto \mathbb{R}$ is a texture containing dense impulse noise. As the time t increases, the solution $p(t, \cdot)$ reflects the gradual diffusion of the initial image I. Both the state of p at the final time T and the entire solution evolution can be regarded as the result.

Numerical solution. For numerical solution, we use the *method of lines* [10], converting the problem (2.1-2.3) to the solution of the system of ODE in the form

$$\frac{\mathrm{d}\boldsymbol{p}}{\mathrm{d}t} = \boldsymbol{f}(t, \boldsymbol{p}). \qquad (2.5)$$

The spatial discretization is carried out by the finite difference method; for the temporal discretization, we employ the 4th-order Runge-Kutta-Merson solver with adaptive time stepping. First, let us introduce the notations

$$\boldsymbol{h} = (h^1, h^2), \ h^k := \frac{L^k}{m^k}, \ k \in \{1, 2\}, \ m_k \in \mathbb{N},$$

$$\boldsymbol{x}_{i,j} = (x_i^1, x_j^2) = (i \cdot h^1, j \cdot h^2),$$

$$\omega_h = \left\{ \boldsymbol{x}_{i,j} \big| i = 1, ..., m^1 - 1, \ j = 1, ..., m^2 - 1 \right\},$$

$$\bar{\omega}_h = \left\{ \boldsymbol{x}_{i,j} \big| i = 0, ..., m^1, \ j = 0, ..., m^2 \right\}, \ \gamma_h = \bar{\omega}_h - \omega_h,$$

$$\mathcal{H}_h = \left\{ u \big| u : \bar{\omega}_h \to \mathbb{R} \right\}, \ u_{i,j} = u(\boldsymbol{x}_{i,j}), \qquad (2.6)$$

$$\mathcal{P}_h w = w \big|_{\bar{\omega}_h} \in \mathcal{H}_h \text{ defined for any } w : \Omega \mapsto \mathbb{R}.$$

The original first order scheme. In the sense of (2.6), we introduce the following forward and backward difference quotients substituted for the partial derivatives of $\partial_{x^1} u$, $\partial_{x^2} u$:

$$u_{\bar{x}^1,i,j} = \frac{u_{i,j} - u_{i-1,j}}{h^1} \quad , \quad u_{x^1,i,j} = \frac{u_{i+1,j} - u_{i,j}}{h^1},$$

$$u_{\bar{x}^2,i,j} = \frac{u_{i,j} - u_{i,j-1}}{h^2} \quad , \quad u_{x^2,i,j} = \frac{u_{i,j+1} - u_{i,j}}{h^2}.$$

Using the above expressions, we can continue in defining the "single directional" discrete substitutes for gradient and divergence:

$$\bar{\nabla}_h u = (u_{\bar{x}^1}, u_{\bar{x}^2}) \quad , \quad \nabla_h u = (u_{x^1}, u_{x^2}),$$

$$\nabla_h \cdot \boldsymbol{V} = V_{x^1}^1 + V_{x^2}^2, \ \bar{\nabla}_h \cdot \boldsymbol{V} = V_{\bar{x}^1}^1 + V_{\bar{x}^2}^2, \ \boldsymbol{V} = \left(V^1, V^2 \right)^{\mathrm{T}}.$$

Finally, we assemble the semi-discrete scheme of the problem (2.1-2.3) for the unknown grid function $p^h : \mathcal{J} \to \mathcal{H}_h$ which represents the vector of functions of time $\boldsymbol{p}$ in (2.5):

$$\xi \frac{\mathrm{d}p^h}{\mathrm{d}t} + \xi \mathcal{P}_h(\boldsymbol{v}) \cdot \bar{\nabla}_h p^h = \xi \nabla_h \cdot T^0(\bar{\nabla}_h p^h) + \frac{1}{\xi} f_0(p^h) + c_0 F \qquad \text{in } \mathcal{J} \times \omega_h, \quad (2.7)$$

$$p^h|_{\gamma_h} = 0 \qquad\qquad\qquad\qquad\qquad \text{on } \mathcal{J} \times \gamma_h, \quad (2.8)$$

$$p^h(0) = \mathcal{P}_h I \qquad\qquad\qquad\qquad\qquad \text{in } \omega_h. \quad (2.9)$$

This scheme will be referred to as the *original scheme*, since it has been used as the starting point for further improvements. In most computational studies, the Dirichlet boundary condition (2.8) has been replaced by the zero Neumann boundary condition.

Weighted numerical scheme. The scheme (2.7-2.9) is of first order in space and suffers from artificial numerical isotropic diffusion, which in accordance with the Fourier error analysis theory [7] affects structures in p^h containing high frequencies. As a result, the formation of streamlines is degraded. However, due to the asymmetry of the scheme, the amount of additional isotropic diffusion depends on the direction of the vector field $\boldsymbol{v}$. This property of the scheme has been exploited to design mixed forward/backward difference quotients approximating the gradient and the divergence by

$$\widetilde{\nabla}_h u = (u_{\bar{x}^1}, u_{x^2})^{\mathrm{T}}, \qquad\qquad \widetilde{\nabla}_h \cdot V = V^1_{\bar{x}^1} + V^2_{x^2},$$

$$\widehat{\nabla}_h u = (u_{x^1}, u_{\bar{x}^2})^{\mathrm{T}}, \qquad\qquad \widehat{\nabla}_h \cdot V = V^1_{x^1} + V^2_{\bar{x}^2}.$$

These expressions allow four versions of discretization of the term $\nabla \cdot T^0 (\nabla p)$ in (2.1), as listed in Figure 2.1. Two complementary scheme asymmetries are obtained, with two perpendicular directions of $\boldsymbol{v}$ corresponding to the weakest numerical diffusion. These directions coincide with the connecting line between the diagonal points used in the respective scheme and can be denoted by

$$\boldsymbol{v}_- = (1, -1)^{\mathrm{T}}, \ \boldsymbol{v}_\sim = (1, 1)^{\mathrm{T}}.$$

Finally, all discretization versions are combined into a single scheme, weighting them by γ_1, γ_2 according to the direction of the vector field:

$$\frac{\gamma_1}{2} \left(\nabla_h \cdot T^0(\bar{\nabla}_h p^h) + \bar{\nabla}_h \cdot T^0(\nabla_h p^h) \right) + \frac{\gamma_2}{2} \left(\widehat{\nabla}_h \cdot T^0(\widetilde{\nabla}_h p^h) + \widetilde{\nabla}_h \cdot T^0(\widehat{\nabla}_h p^h) \right).$$
$$(2.10)$$

The weights are chosen as projections of $\boldsymbol{v}$ into the directions $\boldsymbol{v}_-$ and $\boldsymbol{v}_\sim$ and normalized such that $\gamma_1 + \gamma_2 = 1$, i.e.

$$\tilde{\gamma}_1 = (\mathcal{P}_h \boldsymbol{v}) \cdot \boldsymbol{v}_- = \mathcal{P}_h v^1 - \mathcal{P}_h v^2,$$
$$\tilde{\gamma}_2 = (\mathcal{P}_h \boldsymbol{v}) \cdot \boldsymbol{v}_\sim = \mathcal{P}_h v^1 + \mathcal{P}_h v^2,$$
$$\gamma_1 = \frac{|\tilde{\gamma}_1|}{|\tilde{\gamma}_1| + |\tilde{\gamma}_2|},$$
$$\gamma_2 = \frac{|\tilde{\gamma}_2|}{|\tilde{\gamma}_1| + |\tilde{\gamma}_2|}.$$

As a result, the weighted scheme always prefers the discretization version with the weaker numerical diffusion. The improvement can be observed in Figures 2.2 and 2.3. In (2.10), averaging both discretization versions corresponding to the same direction $\boldsymbol{v}_-$ (or $\boldsymbol{v}_\sim$ respectively) results in a smoothing effect making the scheme more robust with respect to discontinuities in the solution. More visualization results obtained by the weighted scheme are shown in Figure 2.4.

Theoretical convergence results. The work [11] contains a detailed convergence analysis of the original numerical scheme (2.7-2.9), proving the following theorem:
Theorem. *Let $I \in \mathrm{H}^1_0(\Omega) \cap \mathrm{C}(\bar{\Omega})$, $\boldsymbol{v} \in \mathrm{C}(\bar{\Omega})^2$. Then the solution p^h of the semidiscrete scheme (2.7-2.9) converges in $\mathrm{L}_2(\mathcal{J}; \mathrm{L}_2(\Omega))$ to the unique weak solution p of the vector field visualization problem (2.1-2.3), where p satisfies*

$$p \in \mathrm{L}_2(\mathcal{J}; \mathrm{H}^1_0(\Omega)),$$
$$\frac{\partial p}{\partial t} \in \mathrm{L}_2(\mathcal{J}; \mathrm{L}_2(\Omega)).$$

The proof is based on interpolation theory, suitable a priori estimates and the method of compactness.

Experimental proof of convergence. In addition to the theoretical results, the measurement of the experimental order of convergence (EOC) has been performed for both the original and the weighted schemes. EOC is obtained by computing the
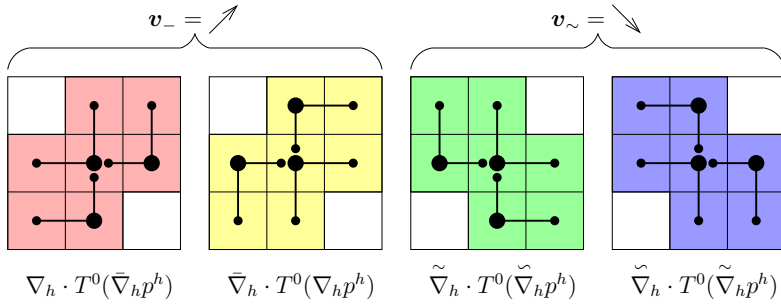
$$\nabla_h \cdot T^0(\bar{\nabla}_h p^h) \qquad \bar{\nabla}_h \cdot T^0(\nabla_h p^h) \qquad \widetilde{\nabla}_h \cdot T^0(\widehat{\widetilde{\nabla}}_h p^h) \qquad \widehat{\widetilde{\nabla}}_h \cdot T^0(\widetilde{\nabla}_h p^h)$$

Fig. 2.1: Versions of $\nabla \cdot T^0\,(\nabla p)$ discretization used for assembling the weighted scheme. Note that the y axis is oriented as on a computer screen, i.e. the y coordinate increases downwards.
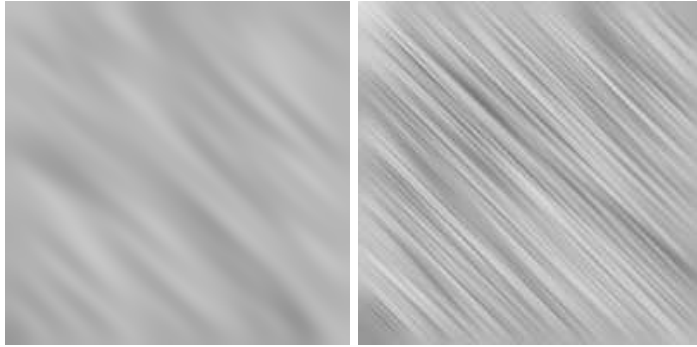

Fig. 2.2: Visualization of the straight vector field in the direction corresponding to the strongest artificial diffusion in the original scheme. Result obtained by the original scheme (2.7-2.9) (left) and by the weighted scheme (right). All parameters were identical for both computations.

solution on a sequence of gradually refining grids and is defined as

$$\mathrm{EOC}_i = \log\left(\frac{\mathrm{Error}_i}{\mathrm{Error}_{i-1}}\right) \Big/ \log\left(\frac{\|\boldsymbol{h}_i\|}{\|\boldsymbol{h}_{i-1}\|}\right),$$

where $\|\boldsymbol{h}\| = \max_j h^j$ is the mesh size and Error_i is the difference of the i-th solution from the precise solution measured in an appropriate norm. As the precise solution is often unknown, one may replace it by the numerical solution on a very fine mesh. The results indicating convergence are summarized in Table 2.1 and Table 2.2.

3. Tensor field visualization problem.

Medical examination of human brain by means of Magnetic Resonance Diffusion Tensor Imaging (MR-DTI) [5, 8] generates a tensor field $\boldsymbol{D} : \bar{\Omega} \mapsto \mathbb{R}^{3\times3}$ where $\Omega \subset \mathbb{R}^3$. In a way similar to the vector field visualization technique dealt with in the previous sections, the tensor field can be processed using the problem for the Allen-Cahn
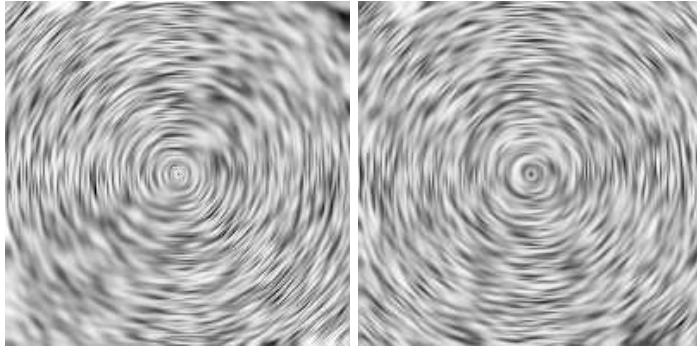
Fig. 2.3: Visualization of the revolving flow. Result obtained by the original scheme (2.7-2.9) (left) and by the weighted scheme (right). All parameters were identical for both computations. The left image clearly indicates the direction most affected by artificial diffusion.
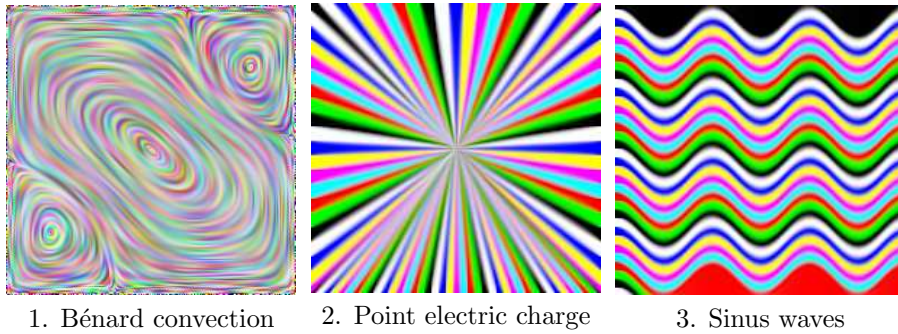

1. Bénard convection   2. Point electric charge   3. Sinus waves

Fig. 2.4: Additional examples of vector field visualization, using RGB component-wise solution. In images 2 and 3, stripe-like Dirichlet boundary conditions together with strong advection were used.

equation described below. The resulting streamlines demonstrated in a 3D texture can be interpreted as neural fiber tracts [14].

Formulation. Consider the time interval $\mathcal{J}$, the domain Ω in the form of a block and a symmetric positive definite diffusion tensor field $\boldsymbol{D}$ representing the input data. The initial boundary value problem for the Allen-Cahn equation reads

$$\xi \frac{\partial p}{\partial t} = \xi \nabla \cdot \tilde{\boldsymbol{D}} \nabla p + \frac{1}{\xi} f_0(p) \qquad \text{in } \mathcal{J} \times \Omega, \qquad (3.1)$$

$$\left. \frac{\partial p}{\partial n} \right|_{\partial \Omega} = 0 \qquad \text{on } \mathcal{J} \times \partial \Omega, \qquad (3.2)$$

$$p|_{t=0} = I \qquad \text{in } \Omega. \qquad (3.3)$$

For the meaning of the symbols p, I, f_0, ξ see section 2.

Numerical solution and reduction of artificial dissipation. Again, the method of lines is utilized for the numerical solution of the problem (3.1-3.3). As in

$\|\boldsymbol{h}\|$	$L_\infty(\mathcal{J}; L_2(\Omega))$ error	EOC in $L_\infty(\mathcal{J}; L_2(\Omega))$	$L_\infty(\mathcal{J}; L_\infty(\Omega))$ error	EOC in $L_\infty(\mathcal{J}; L_\infty(\Omega))$
1.000E-02	2.578E-02	-	2.909E-01	-
5.000E-03	8.218E-03	1.650E+00	1.145E-01	1.345E+00
2.500E-03	2.755E-03	1.577E+00	4.659E-02	1.298E+00
1.250E-03	7.728E-04	1.834E+00	1.333E-02	1.805E+00

Table 2.1: EOC results for the original scheme (2.7-2.9).

$\|\boldsymbol{h}\|$	$L_\infty(\mathcal{J}; L_2(\Omega))$ error	EOC in $L_\infty(\mathcal{J}; L_2(\Omega))$	$L_\infty(\mathcal{J}; L_\infty(\Omega))$ error	EOC in $L_\infty(\mathcal{J}; L_\infty(\Omega))$
1.000E-02	2.499E-02	-	2.057E-01	-
5.000E-03	7.302E-03	1.775E+00	6.335E-02	1.699E+00
2.500E-03	2.284E-03	1.677E+00	1.968E-02	1.686E+00
1.250E-03	6.455E-04	1.823E+00	6.090E-03	1.693E+00

Table 2.2: EOC results for the weighted scheme (2.10).

the previous case, the artificial diffusion resulting from spatial discretization has to be dealt with.

The streamlines emerging in the solution are thin high frequency structures. Recalling the Fourier analysis [7], the number of *grid points per wave* (*PPW*) can be estimated for each difference operator. Depending on the spectrum of the solution, this quantity defines the grid density necessary to produce an approximation error below the desired level. As *PPW* decreases significantly with the order of the difference operator, we obtain two general possibilities of artificial diffusion reduction: increasing the order of approximation and/or refining the grid. However, due to the CPU and memory requirements of the computation on a 3D grid, the latter is not an option.

Hence, a higher order scheme of the finite volume (FV) method [6] on a rectangular structured grid has been chosen, yielding a semidiscrete scheme in the form

$$\xi \partial_t p(t) = \xi \sum_{\sigma \in \mathcal{E}_K} F_{K,\sigma}(t) + \frac{1}{\xi} f_{0,K}(t), \qquad (3.4)$$

where $\mathcal{E}_K$ is the set of all faces of the cell K. $F_{K,\sigma}(t)$ are the respective numerical fluxes at the time t, which contain difference quotients observing a symmetric 5-point stencil and approximating the derivatives $\partial_x p$, $\partial_y p$, $\partial_z p$ at the center of the face σ.

- The difference quotient approximating the derivative in the direction perpendicular to the face σ uses a non-equidistant point distribution in order to prevent redundant interpolation (Figure 3.1a).
- The remaining derivatives are approximated using a uniform 5-point stencil. The stencil points (the crosses along the dashed line in Figure 3.1b) are interpolated from the neighboring grid nodes using 1-dimensional cubic interpolation.

The results of the experimental convergence analysis are summarized in Table 3.1. As for artificial diffusion, the comparison of four schemes restricted to $\mathbb{R}^2$ is shown in

h	$L_\infty(\mathcal{J}; L_2(\Omega))$ error	EOC in $L_\infty(\mathcal{J}; L_2(\Omega))$	$L_\infty(\mathcal{J}; L_\infty(\Omega))$ error	EOC in $L_\infty(\mathcal{J}; L_\infty(\Omega))$
1.020E-02	1.806E-04	–	3.798E-03	–
5.102E-03	6.137E-05	1.557E+00	1.188E-03	1.675E+00
2.551E-03	1.828E-05	1.747E+00	5.256E-04	1.177E+00

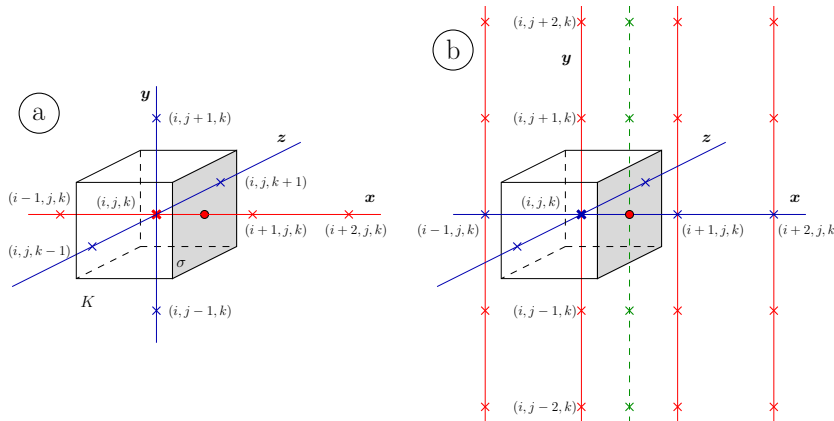Table 3.1: EOC results for the higher order FV scheme.   Mesh size $h = \max_K \mathrm{diam}(K)$.

Fig. 3.1: Difference quotients in derivative approximations in the FV scheme (3.4).

Figure 3.2. In both cases, the initial condition depicted on the very left underwent a process of anisotropic diffusion directed along the axis $y = x$.

4. Conclusion.

In problems of vector field or tensor field visualization, we come across the necessity of reducing the level of artificial dissipation (isotropic diffusion) generated by the numerical scheme. Two possibilities of overcoming this difficulty were described; either a specific modification of the numerical scheme can be designed, exploiting its properties, or a more general solution in the form of the higher order scheme can be adopted. The presented results prove that both techniques were successful in the context of visualization. Other preliminary results indicate that the proposed higher order FVM scheme is still resistant to oscillations. However, more analysis is a matter of further research, as well as the optimal choice of boundary conditions for the higher order scheme.
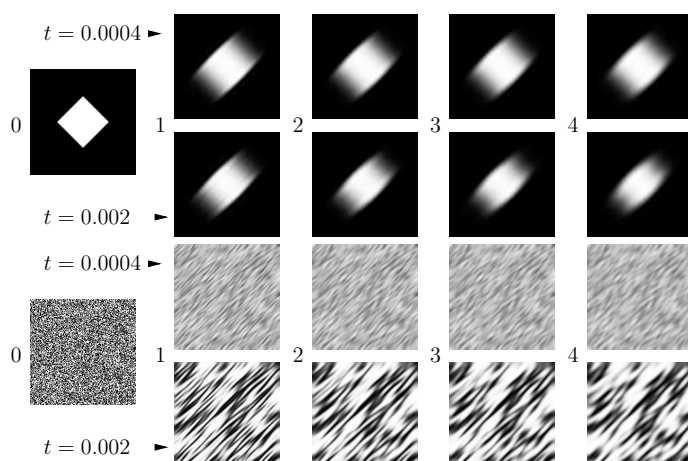
0. Initial condition

1. FV, 5-point (4th order), cubic interpolation   **3.** FV, 2nd order central difference

2. FV, 5-point, linear interpolation   **4.** Finite difference, 1st order forward-backward

Fig. 3.2: Artificial diffusion in different numerical schemes, 2 time levels.

REFERENCES

[1] S. Allen and J. W. Cahn. A microscopic theory for antiphase boundary motion and its application to antiphase domain coarsening. *Acta Metall.*, 27:1084–1095, 1979.

[2] M. Beneš. Mathematical analysis of phase-field equations with numerically efficient coupling terms. *Interfaces and Free Boundaries*, 3:201–221, 2001.

[3] M. Beneš. Diffuse-interface treatment of the anisotropic mean-curvature flow. *Applications of Mathematics*, 48(6):437–453, 2003.

[4] M. Beneš, V. Chalupecký, and K. Mikula. Geometrical image segmentation by the Allen-Cahn equation. *Applied Numerical Mathematics*, 51(2):187–205, 2004.

[5] D. L. Bihan et al. Diffusion tensor imaging: Concepts and applications. *Journal of Magnetic Resonance Imaging*, 13:534–546, 2001.

[6] R. Eymard, T. Gallouët, and R. Herbin. Finite volume methods. In P. G. Ciarlet and J. L. Lions, editors, *Handbook of Numerical Analysis*, volume 7, pages 715–1022. Elsevier, 2000.

[7] H. Lomax, T. H. Pulliam, and D. W. Zingg. *Fundamentals of Computational Fluid Dynamics*. Springer, 2001.

[8] S. Mori and J. Zhang. Principles of diffusion tensor imaging and its applications to basic neuroscience research. *Neuron*, 51:527–539, 2006.

[9] T. Preußer and M. Rumpf. Anisotropic nonlinear diffusion in flow visualization. In *Proceedings of IEEE Visualization 1999*, 1999.

[10] W. E. Schiesser. *The Numerical Method of Lines: Integration of Partial Differential Equations*. Academic Press, San Diego, 1991.

[11] P. Strachota. Anisotropic diffusion in mathematical visualization. Master's thesis, Czech Technical University in Prague, 2007. (in Czech).

[12] P. Strachota. Vector field visualization by means of anisotropic diffusion. In M. Beneš, M. Kimura, and T. Nakaki, editors, *Proceedings of Czech Japanese Seminar in Applied Mathematics 2006*, volume 6 of *COE Lecture Note*, pages 193–205. Faculty of Mathematics, Kyushu University Fukuoka, 2007.

[13] P. Strachota. Anisotropic diffusion in mathematical visualization. In *Science and Supercomputing in Europe - Report 2007*, pages 826–831, Bologna, 2008. CINECA Consorzio Interuniversitario.

[14] D. Tschumperlé and R. Deriche. Tensor field visualization with PDE's and application to DT-MRI fiber visualization. INRIA Sophia-Antipolis, Odyssée Lab, France, 2004.